Radius Constraints from Reflection Modeling of Cygnus X-2 with NuSTAR and NICER

R. M. Ludlam, E. M. Cackett, J. A. García, J. M. Miller, A. L. Stevens, A. C. Fabian, J. Homan, M. Ng, S. Guillot, D. J. K. Buisson, et al.

The Astrophysical Journal, 927:112 (11pp), 2022 March 1 https://doi.org/10.3847/1538-4357/ac5028

Radius Constraints from Reflection Modeling of Cygnus X-2 with NuSTAR and NICER

R. M. Ludlam[1,11], E. M. Cackett[2], J. A. García[1], J. M. Miller[3], A. L. Stevens[3,4], A. C. Fabian[5], J. Homan[6], M. Ng[7], S. Guillot[8,9], D. J. K. Buisson[10], and D. Chakrabarty[7]
[1] Cahill Center for Astronomy and Astrophysics, California Institute of Technology, Pasadena, CA 91125, USA; rmludlam@caltech.edu
[2] Department of Physics & Astronomy, Wayne State University, 666 West Hancock Street, Detroit, MI 48201, USA
[3] Department of Astronomy, University of Michigan, 1085 South University Ave, Ann Arbor, MI 48109-1107, USA
[4] Department of Physics & Astronomy, Michigan State University, 567 Wilson Road, East Lansing, MI 48824, USA
[5] Institute of Astronomy, Madingley Road, Cambridge, CB3 0HA, UK
[6] Eureka Scientific, Inc., 2452 Delmer Street, Oakland, CA 94602, USA
[7] MIT Kavli Institute for Astrophysics and Space Research, Massachusetts Institute of Technology, Cambridge, MA 02139, USA
[8] CNRS, IRAP, 9 avenue du Colonel Roche, BP 44346, F-31028 Toulouse Cedex 4, France
[9] Université de Toulouse, CNES, UPS-OMP, F-31028 Toulouse, France
[10] Department of Physics and Astronomy, University of Southampton, Highfield, Southampton, SO17 1BJ, UK
Received 2021 October 20; revised 2022 January 6; accepted 2022 January 27; published 2022 March 9

Abstract

We present a spectral analysis of NuSTAR and NICER observations of the luminous, persistently accreting neutron star (NS) low-mass X-ray binary Cygnus X-2. The data were divided into different branches that the source traces out on the Z-track of the X-ray color–color diagram; namely, the horizontal branch, the normal branch, and the vertex between the two. The X-ray continuum spectrum was modeled in two different ways that produced comparable quality fits. The spectra showed clear evidence of a reflection component in the form of a broadened Fe K line, as well as a lower-energy emission feature near 1 keV likely due to an ionized plasma located far from the innermost accretion disk. We account for the reflection spectrum with two independent models (RELXILLNS and RDBLUR*RFXCONV). The inferred inclination is in agreement with earlier estimates from optical observations of ellipsoidal lightcurve modeling (RELXILLNS: $i = 67^\circ \pm 4^\circ$; RDBLUR*RFXCONV: $i = 60^\circ \pm 10^\circ$). The inner disk radius remains close to the NS ($R_{\rm in} \leqslant 1.15\ R_{\rm ISCO}$) regardless of the source position along the Z-track or how the 1 keV feature is modeled. Given the optically determined NS mass of $1.71 \pm 0.21\ M_\odot$, this corresponds to a conservative upper limit of $R_{\rm in} \leqslant 19.5$ km for $M = 1.92\ M_\odot$ or $R_{\rm in} \leqslant 15.3$ km for $M = 1.5\ M_\odot$. We compare these radius constraints to those obtained from NS gravitational wave merger events and recent NICER pulsar lightcurve modeling measurements.

Unified Astronomy Thesaurus concepts: Neutron stars (1108); Low-mass x-ray binary stars (939); Accretion (14)

1. Introduction

Measuring neutron star (NS) masses and radii remains crucial for determining the equation of state (EoS) of ultradense, cold matter (Lattimer & Prakash 2001). Numerous observational methods have been developed for obtaining NS mass and/or radius (Özel & Freire 2016) in order to narrow down the allowed region on the mass–radius (M–R) plane and rule out theoretical models. Notably, enticing breakthroughs have been made via measuring the tidal deformability of NSs from the gravitational wave signature during NS–NS binary merger events (e.g., GW170817: Abbott et al. 2019), as well as determining the compactness of millisecond pulsars through lightcurve modeling of modulations from hot spots on the NS surface as they rotate into and out of our line of sight (e.g., PSR J0030: Miller et al. 2019; Riley et al. 2019).

An additional method of independently determining NS radii can be obtained from modeling the reprocessed emission from the innermost accretion disk that has been externally illuminated. This is commonly referred to as the "reflection" spectrum, which has a series of narrow emission lines superimposed on a reprocessed continuum. Emission from the inner disk region (most prominently seen in the Fe K line) is broadened due to Doppler, general, and special relativistic effects (Fabian et al. 1989, 2000), which allows for a measurement of the position of the inner edge of the disk. Since the accretion disk must truncate at or prior to the NS surface, determining the inner disk radius provides a limit on the radius of the NS (Cackett et al. 2008; Ludlam et al. 2017).

One system that has potential for demonstrating the power of NS reflection studies is the luminous, persistently accreting low-mass X-ray binary (LMXB) Cygnus X-2 (Cyg X-2), especially since it has an optically determined mass. The source was first observed in the X-rays via a sounding rocket in the 1960s (Byram et al. 1966). Cyg X-2 was tentatively classified as an NS when a weak X-ray burst was observed with the Einstein Observatory (Kahn & Grindlay 1984), and was later confirmed when RXTE observed a Type-I X-ray burst while the source was in a high-intensity state (Smale 1998). Cyg X-2 is classified as a "Z" source based on the tracks traced out in hardness and color–color diagrams (Hasinger & van der Klis 1989). However, the exact shape and location on these diagrams varies, depending on the overall intensity level (Kuulkers et al. 1996; Wijnands et al. 1997; Fridriksson et al. 2015), which can vary by a factor of ∼4 (Wijnands & van der Klis 2001). The neutral hydrogen column density along the line of sight is low ($N_{\rm H} \sim 2 \times 10^{21}$ cm^{-2}: HI4PI Collaboration et al. 2016) with the abundance of oxygen being slightly supersolar ($A_{\rm O}/A_\odot = 1.1$: Psaradaki et al. 2020).

[11] NASA Einstein Fellow.

Due to the low column density, the source has been observed extensively in the optical as well. The stellar companion is an evolved, late-type A9III star in a 9.8444 ± 0.0003 day orbit (Casares et al. 1998). From modeling of ellipsoidal lightcurves, the mass function of the system was estimated as $f(M) = 0.66 \pm 0.03\ M_{\odot}$ (Casares et al. 2010), which led to an estimate of the NS mass of $1.71 \pm 0.21\ M_{\odot}$ for an inclination of $62.^{\circ}5 \pm 4^{\circ}$ (Orosz & Kuulkers 1999). Cyg X-2 is estimated to be located at a distance of 8–11 kpc (Cowley et al. 1979; Smale 1998), though optical observations tend toward the lower end of this (7.2 ± 1.1 kpc: Orosz & Kuulkers 1999). More recently, Ding et al. (2021) estimated a distance of $11.3^{+0.9}_{-0.8}$ kpc using a Bayesian inference approach that utilized information from Gaia Early Data Release 3 and photospheric radius expansion bursts.

Due to the luminous and persistent nature of the source, the spectral properties have been studied considerably. The source spectrum is known to show a broad Fe line feature near 6.7 keV (Smale et al. 1993; Di Salvo et al. 2002; Shaposhnikov et al. 2009; Cackett et al. 2010; Mondal et al. 2018) due to reflection from the accretion disk, as well an emission line near 1 keV (Vrtilek et al. 1986; Chiappetti et al. 1990; Smale et al. 1993; Kuulkers et al. 1997; Di Salvo et al. 2002; Farinelli et al. 2009; Cackett et al. 2010) that likely originates from collisionally excited or photoionized material farther out in the disk (Vrtilek et al. 1986). The source traces out the horizontal, normal, and flaring branches of the "Z" with periods of irregular dipping activity while flaring; suggesting the presence of an extended accretion disk corona during high-intensity states (Vrtilek et al. 1988; Schulz et al. 2009; Bałucińska-Church et al. 2010, 2011). A detailed broadband spectral analysis of Cyg X-2 with BeppoSAX while the source was in the horizontal and normal branches was reported in Di Salvo et al. (2002). The continuum modeling suggested that the inner accretion disk moved closer to the NS as the inferred mass accretion rate increased as the source transitioned from the horizontal to the normal branch, but a full treatment of the reflection spectrum was not conducted.

Reflection modeling of Suzaku observations was performed in Cackett et al. (2010) using a DISKLINE component and blackbody reflection model (BBREFL) to obtain inner disk radius and inclination constraints. The disk was inferred to be close to the NS at $R_{\rm in} \simeq 7.6$–$8.5\ R_g$ (where $R_g = GM/c^2$) when using a single DISKLINE component, and $R_{\rm in} \simeq 6 - 14\ R_g$ when using the full reflection model. Mondal et al. (2018) recently analyzed a NuSTAR observation of Cyg X-2 in the normal branch and flaring/dipping state. The reflection component was modeled with a different blackbody reflection model, known as REFLIONXBB, and the disk was inferred to be far from the NS at $R_{\rm in} \simeq 13.5$–$32.4\ R_g$ in the nondipping state. The inferred inclinations in both of these studies ($i \lesssim 25^{\circ}$), however, are at odds with the inclination measured from optical observations. This may be due to the thickness of the disk in the outer regions being able to partially obscure the blue-winged emission of the Fe K line (Taylor & Reynolds 2018).

Here, we analyze the existing NuSTAR observations of Cyg X-2 while the source is in a nondipping state in order to carefully obtain radius constraints from reflection modeling. Though one NuSTAR observation was reported on in Mondal et al. (2018), two additional NuSTAR observations were performed simultaneously with NICER. Hence, we present the results of joint NICER and NuSTAR spectral modeling. The organization of the paper is as follows: Section 2 presents the observations and data reduction methodology; Section 3 reports the spectral modeling and results; Section 4 discusses the results and compares them to the current best constraints on NS mass and radius; and Section 5 then provides the conclusion.

Table 1
Observation Information

Obs #	Mission	Sequence ID	Obs. Start Date	Exp. (ks)
1	NuSTAR	30001141002	2015-01-07 03:16:07	∼23.7
2	NuSTAR	80511301002	2019-09-10 13:06:09	∼11.3
	NICER	2631010101	2019-09-10 12:58:20	∼12.7
3	NuSTAR	80511301004	2019-09-12 02:06:09	∼12.7
	NICER	2631010201	2019-09-12 02:09:44	∼12.1

2. Observations and Data Reduction

NuSTAR has observed Cyg X-2 on three occasions. The sequence IDs, observation dates, and exposure times are given in Table 1. All data were reduced using CALDB v.20210427 and "nupipeline" with "statusexpr"STATUS == b0000xxx00xxxx000,"" due to the source brightness having an excess of 100 counts s^{-1}. The background filtering report for Obs1 indicated periods of high background, hence we applied "saacalc = 3 saamode = optimized tentacle = yes." Source regions of 100″ radii centered on the source and a background region of the same size but sufficiently far from the source were used for spectra and lightcurve extraction. The lightcurves were inspected for Type-I X-ray bursts, but none were present. The hardness ratio (HR: 10–16 keV/6.4–10 keV) versus 3–20 keV intensity, known as the hardness–intensity diagram (HID), is shown in Figure 1, as well as the lightcurves and hardness ratio (HR) versus time for each NuSTAR observation. The observations trace out the flaring to the horizontal branch in the HID, and show shifts in the overall intensity between the 2015 and 2019 observations.

NICER observed the source simultaneously with NuSTAR during Obs2 and Obs3. Information for each sequence ID is given in Table 1. Data were reduced and calibrated using the standard "nicerl2" command and CALDB version 20200722. Additionally, the data were filtered to select for KP < 5 and COR_SAX > 4 to mitigate the particle background at low energies. The simultaneous lightcurves for these observations are shown in Figure 2, where the zero-point indicates the start of the NICER observation for Obs2 and the beginning of the NuSTAR observation for Obs3. No Type-I X-ray bursts were present in the NICER data.

The NuSTAR and NICER data were divided into different branches within each observation using good time intervals (GTIs) based on the HIDs and lightcurves shown in Figures 1 and 2. The source went through the normal to extended flaring branch in Obs1 while in the high-intensity state, as reported in Mondal et al. (2018). We divide the data in a similar manner by separating the nondip emission from the dipping by creating GTIs that divide the observation at $t = 45$ ks. Obs2 and Obs3 occurred while the source was in a lower-intensity state. Obs2 traced out the upper normal branch (NB), the vertex (VX), and the horizontal branch (HB). The HB occurred from $t < 7.5$ ks, the NB from $t = 21.5$–27.5 ks, and the VX from $t = 7.5$–21.5 ks and $t > 27.5$ ks. Obs3 occurred as the source was exiting a dipping period. Therefore, the first 5 ks were removed. The remaining data were divided between the NB ($t = 5$–10 ks) and HB ($t > 10$ ks). These GTIs were applied to

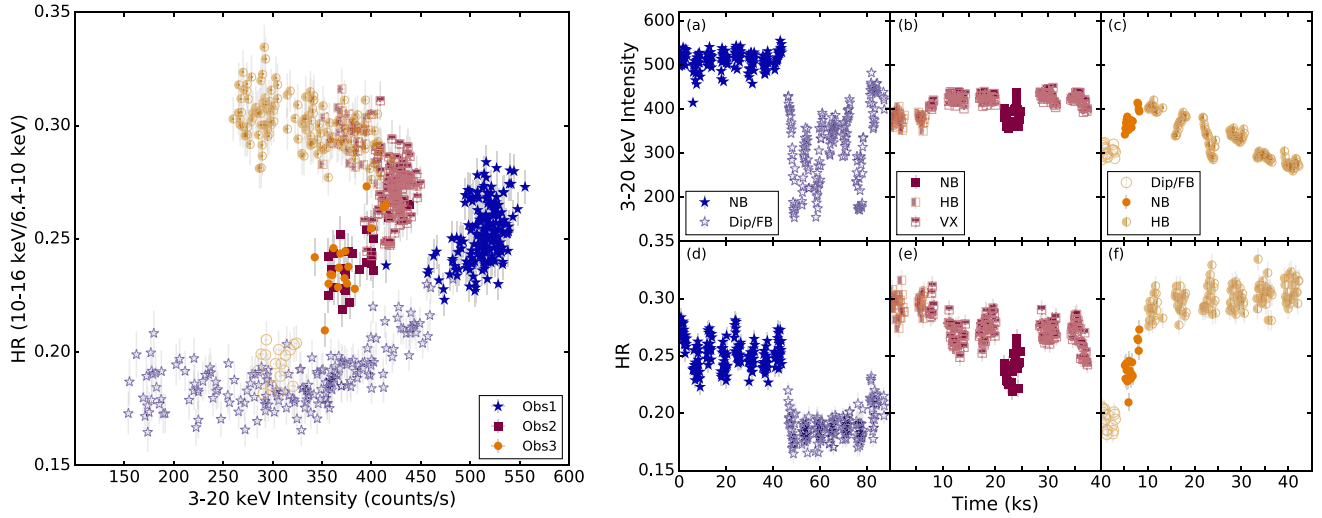

Figure 1. Left: the NuSTAR HR vs. the 3–20 keV intensity. The shapes of the symbols indicate the observations. The variations in coloring and shading between the symbols indicate the spectral state, where solid is the NB, the top half being filled is the VX, the left half being filled is the HB, and open indicates where the source is dipping or in the flaring branch (Dip/FB). Right: the top row shows the NuSTAR 3–20 keV lightcurve of Cyg X-2 for (a) Obs1, (b) Obs2, and (c) Obs3. The lower panels show the HRs during the observations. The coloring/shading of the symbols are coded based on the HID. Data were binned to 128 s.

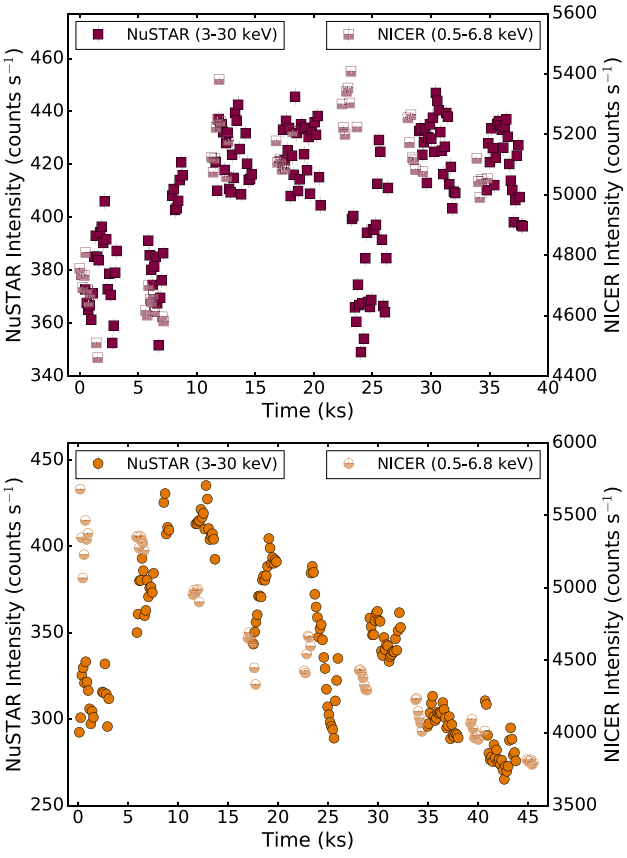

Figure 2. The lightcurves of the simultaneous NuSTAR and NICER observations of Cyg X-2 for Obs2 (the upper panel) and Obs3 (the lower panel). Data were binned to 128 s.

the NuSTAR data through "nuproducts" to extract spectra while the data were in the NB, HB, and VX. The NICER data were divided into these different branches by converting the NuSTAR GTIs into NICER mission elapsed time, and then extracting the corresponding events through "niextract-events." The source and background spectra for the NICER data were created using the "3C50" tool[12] (Remillard et al. 2022).

3. Spectral Modeling and Results

We utilize XSPEC v12.11.1 to model all spectra simultaneously. To account for the cross-calibration difference between NICER and NuSTAR, we use the CRABCORR multiplicative model (a.k.a. JSCRAB; Steiner et al. 2010). This model has two parameters: (1) $\Delta\Gamma$, which multiplies the spectrum by a power-law difference ($E^{-\Delta\Gamma}$); and (2) a normalization, C, which serves in the same capacity as a multiplicative constant. $\Delta\Gamma$ is set to 0 for the NuSTAR spectra and allowed to float for the NICER spectra. Although the value of $\Delta\Gamma$ is small, it is important to account for unavoidable mission-specific calibration differences that emerge when the Crab is observed. The multiplicative constant was allowed to vary for the FPMB and NICER, while the FPMA was fixed at unity. The absorption column along the line of sight was modeled with TBFEO, with abundances set to WILM (Wilms et al. 2000) and VERN (Verner et al. 1996) cross sections. The column density, $N_{\rm H}$, and abundance of oxygen, $A_{\rm O}$, were allowed to vary but tied between all spectra regardless of spectral state. Errors are reported at the 90% confidence level from a Markov Chain Monte Carlo with 50 walkers, a burn-in of 1×10^6, and a chain length of 5×10^4.

In the interest of obtaining robust constraints on the inner disk radius, we focus on modeling the nondipping spectra that have $\geqslant 10^6$ cumulative counts per spectrum. This corresponds to the NuSTAR spectra of Obs1 in the NB, the NICER and NuSTAR spectra of Obs2 in the VX, and the NICER and NuSTAR spectra of Obs3 in the HB. These will be referred to by their branch nomenclature in Tables 2–4. We model the continuum with the phenomenological three-component model of Lin et al. (2007). This model is comprised of a multitemperature blackbody to account for the thermal disk emission (DISKBB: Mitsuda et al. 1984), a single-temperature blackbody (BBODY) for emission from the NS surface or boundary layer

[12] https://heasarc.gsfc.nasa.gov/docs/nicer/tools/nicer_bkg_est_tools.html

Table 2
Continuum Spectral Modeling

Model	Parameter	C1			C2		
		NB	VX	HB	NB	VX	HB
CRABCOR	$C_{\rm FPMB}$	1.022 ± 0.001	$1.014^{+0.001}_{-0.002}$	$1.013^{+0.002}_{-0.001}$	$1.013^{+0.003}_{-0.001}$	$1.014^{+0.002}_{-0.001}$	$1.022^{+0.002}_{-0.001}$
	$C_{\rm NICER}$	⋯	0.99 ± 0.01	1.02 ± 0.01	⋯	1.01 ± 0.01	0.98 ± 0.01
	$\Delta\Gamma_{\rm NICER}$[b] (10^{-2})	⋯	$-4.4^{+0.6}_{-0.4}$		⋯	$-5.1^{+0.7}_{-0.4}$	
TBFEO	$N_{\rm H}$[a] (10^{21} cm^{-2})	⋯	$4.19^{+0.13}_{-0.06}$	⋯	⋯	$2.2^{+0.1}_{-0.2}$	⋯
	$A_{\rm O}$[a]	⋯	$1.09^{+0.04}_{-0.03}$	⋯	⋯	$1.32^{+0.07}_{-0.02}$	⋯
DISKBB	$kT_{\rm in}$ (keV)	1.76 ± 0.01	1.80 ± 0.01	1.78 ± 0.01	1.72 ± 0.01	1.80 ± 0.01	$1.83^{+0.02}_{-0.01}$
	$\rm norm_{disk}$	119^{+4}_{-2}	83^{+2}_{-1}	60 ± 1	110^{+2}_{-6}	69 ± 2	41^{+1}_{-2}
BBODY	$kT_{\rm bb}$ (keV)	$2.68^{+0.01}_{-0.03}$	$2.72^{+0.03}_{-0.02}$	2.67 ± 0.02	⋯	...	...
	$\rm norm_{bb}$ (10^{-2})	$3.37^{+0.14}_{-0.07}$	3.6 ± 0.1	$3.71^{+0.07}_{-0.09}$	⋯	...	...
POWERLAW	Γ	$3.96^{+0.04}_{-0.09}$	$3.19^{+0.11}_{-0.01}$	$2.99^{+0.06}_{-0.04}$	⋯	...	...
	$\rm norm_{pl}$	7 ± 1	1.5 ± 0.1	1.6 ± 0.1	⋯	...	...
NTHCOMP	Γ	⋯	...	⋯	$1.77^{+0.06}_{-0.02}$	$1.69^{+0.03}_{-0.02}$	$1.78^{+0.02}_{-0.01}$
	kT_e (keV)	⋯	...	⋯	$2.89^{+0.05}_{-0.02}$	$3.03^{+0.03}_{-0.04}$	$3.11^{+0.05}_{-0.01}$
	kT_{bb} (10^{-1} keV)	⋯	...	⋯	$1.27^{+0.07}_{-1.24}$	$1.6^{+0.1}_{-0.4}$	$1.8^{+0.08}_{-0.25}$
	$\rm norm_{nth}$	⋯	...	⋯	$1.35^{+0.27}_{-0.07}$	$0.88^{+0.10}_{-0.05}$	$1.19^{+0.07}_{-0.04}$
	$F_{\rm unabs,0.5-50\ keV}$	5.0 ± 0.3	2.6 ± 0.2	2.1 ± 0.3	3.0 ± 0.2	$2.3^{+0.3}_{-0.1}$	$1.9^{+0.4}_{-0.1}$
	χ^2 (dof)		3380.0 (1952)			3386.8 (1952)	

Notes. Errors are reported at the 90% confidence level. NICER is fit in the 0.5–10 keV energy band while NuSTAR is fit in the 3–30 keV band. A multiplicative constant is used on the NICER and FPMB data, while FPMA is fixed to unity. The input seed photon type in NTHCOMP is set to a single-temperature blackbody (inp_type=0). The BBODY normalization is defined as $(L/10^{39}\ {\rm erg\ s^{-1}})/(D/10\ {\rm kpc})^2$. The DISKBB normalization is defined as $(R_{\rm in}/{\rm km})^2/(D/10\ {\rm kpc})^2 \times \cos\theta$. The power-law normalization is defined as photons keV^{-1} cm^{-2} s^{-1} at 1 keV. The unabsorbed 0.5–50 keV flux, $F_{\rm unabs,0.5-50\ keV}$, is given in units of 10^{-8} erg s^{-1} cm^{-2}.
[a] Tied between all branches.
[b] Tied between NICER spectra.

region, and a power-law (POW) component to model weak Comptonization. This continuum model is referred to as "C1" in Table 2. The ratio of the model to the data are shown in Figure 3(a). Additionally, we swap out the power-law and single-temperature blackbody components for a more physical Comptonization model, NTHCOMP (Zdziarski et al. 1996; Zycki et al. 1999). The parameter values can be found in Table 2 under "C2" and the ratio of the model to the data are shown in Figure 3(b). The fits are of comparable statistical quality, though C1 provides a slightly better fit. The spectral parameters for the NB are relatively consistent with those reported in Mondal et al. (2018), but it is important to note that differences likely arise from the bright source flag being utilized when we reduced the NuSTAR data.

There is clear evidence of a broadened Fe K line component in all spectra regardless of continuum model. Figure 4 shows the Fe line profile in each respective branch. Additionally, there is an emission line present in the NICER spectra at lower energy ($\sim$1 keV). As mentioned in the introduction, this feature has been reported previously with other X-ray missions.

We model the reflected emission in two separate ways corresponding to the input continuum. Starting from C1, we utilize the variation of RELXILL (García et al. 2014) known as RELXILLNS (García et al. 2022) to account for reprocessed emission due to an illuminating blackbody component, kT_{bb}. The model parameters are as follows: an inner emissivity index ($q_{\rm in}$); an outer emissivity index ($q_{\rm out}$); the break radius ($R_{\rm break}$) between the two emissivity indices; dimensionless spin parameter (a); redshift (z); the inclination of the system (i); the inner disk radius ($R_{\rm in}$) in units of the innermost stable circular orbit (ISCO); the outer disk radius ($R_{\rm out}$) in units of gravitational radii (R_g); an ionization parameter ($\log(\xi)$); disk density ($\log(N\,[{\rm cm^{-3}}])$); iron abundance ($A_{\rm Fe}$); and reflection fraction ($f_{\rm refl}$). We tie the inner and outer emissivity indices to create a single emissivity profile, q, and therefore $R_{\rm break}$ becomes irrelevant. Cyg X-2 is a Galactic source, so we fix the redshift parameter to $z = 0$. The outer disk radius is set at 1000 R_g and the spin parameter is fixed at $a = 0$. The choice of spin parameter is motivated by most NSs in LMXBs having $a \lesssim 0.3$ (Galloway et al. 2008; Miller et al. 2011) and the difference in the position of $R_{\rm ISCO}$ between these two values being less than 1 R_g (Ludlam et al. 2018). The reflection fraction, $f_{\rm refl}$, is bound to positive values so that the RELXILLNS model encompasses both the illuminating blackbody from the continuum and the reprocessed reflection emission component. These model fits are reported in Table 3 under "RNS1."

Conversely, when starting from C2, we use the reflection convolution model RFXCONV (Done & Gierlínski 2006) with the relativistic blurring kernal RDBLUR (Fabian et al. 1989) to emulate the reprocessed emission from a Comptonization blackbody with general and special relativistic effects around a nonspinning compact object (i.e., $a = 0$). We choose RDBLUR so that this overall model and RNS1 are completely independent of each other. RFXCONV generates an angle-dependent reflection spectrum from the NTHCOMP input spectrum it is convolved with by combining the Compton-reflected emission from PEXRIV (Magdziarz & Zdziarski 1995) above 14 keV (using the average 12–14 keV power-law index) with the reflection emission from an ionized disk interpolated from REFLIONX (Ross & Fabian 2005) below 14 keV (using the average 2–10 keV power-law index). The reflected emission interpolated from REFLIONX and PEXRIV are scaled to match at 14 keV. The parameters of this convolution model are the relative reflection normalization ($rel_{\rm refl}$), the Fe

Table 3
Reflection Modeling from a Single-temperature Blackbody

Model	Parameter	RNS1			RNS2			RNS3		
		NB	VX	HB	NB	VX	HB	NB	VX	HB
CRABCOR	$C_{\rm FPMB}$	1.022 ± 0.001	1.014 ± 0.002	$1.014^{+0.003}_{-0.001}$	$1.022^{+0.002}_{-0.001}$	1.014 ± 0.002	$1.015^{+0.001}_{-0.003}$	$1.023^{+0.001}_{-0.002}$	1.014 ± 0.002	$1.015^{+0.001}_{-0.002}$
	$C_{\rm NICER}$	⋯	$0.969^{+0.006}_{-0.008}$	$0.996^{+0.005}_{-0.007}$	⋯	$0.974^{+0.007}_{-0.002}$	$1.000^{+0.007}_{-0.002}$	⋯	$0.966^{+0.004}_{-0.007}$	$0.993^{+0.005}_{-0.008}$
	$\Delta\Gamma_{\rm NICER}$[b] (10^{-2})	⋯	-5.7 ± 0.4		⋯	-5.7 ± 0.2		⋯	$-5.8^{+0.2}_{-0.6}$	
TBFEO	$N_{\rm H}$[a] (10^{21} cm^{-2})	⋯	$3.92^{+0.08}_{-0.07}$	⋯	⋯	$3.71^{+0.09}_{-0.05}$	⋯	⋯	$3.65^{+0.14}_{-0.07}$	⋯
	$A_{\rm O}$[a]	⋯	$1.16^{+0.05}_{-0.01}$	⋯	⋯	$1.17^{+0.04}_{-0.03}$	⋯	⋯	$1.19^{+0.03}_{-0.06}$	⋯
DISKBB	$kT_{\rm in}$ (keV)	$1.77^{+0.02}_{-0.01}$	$1.73^{+0.03}_{-0.01}$	$1.65^{+0.01}_{-0.03}$	1.77 ± 0.01	1.73 ± 0.02	$1.61^{+0.04}_{-0.01}$	$1.78^{+0.01}_{-0.02}$	1.74 ± 0.02	$1.63^{+0.02}_{-0.01}$
	$\rm norm_{disk}$	114^{+2}_{-4}	94^{+1}_{-5}	78^{+4}_{-2}	116^{+2}_{-3}	94^{+3}_{-4}	86^{+1}_{-7}	114^{+4}_{-3}	91^{+4}_{-2}	82^{+2}_{-4}
POWERLAW	Γ	$3.43^{+0.08}_{-0.10}$	3.02 ± 0.05	$2.84^{+0.03}_{-0.04}$	$3.41^{+0.01}_{-0.10}$	2.95 ± 0.06	2.79 ± 0.03	$3.44^{+0.01}_{-0.10}$	$2.94^{+0.09}_{-0.04}$	$2.79^{+0.05}_{-0.03}$
	$\rm norm_{pl}$	$5.2^{+0.7}_{-0.4}$	$1.41^{+0.09}_{-0.05}$	$1.49^{+0.08}_{-0.03}$	$4.9^{+0.2}_{-0.3}$	1.19 ± 0.07	$1.26^{+0.10}_{-0.04}$	$4.7^{+0.3}_{-0.2}$	$1.18^{+0.08}_{-0.11}$	$1.23^{+0.12}_{-0.05}$
RELXILLNS	q	$2.19^{+0.10}_{-0.09}$	1.8 ± 0.1	1.8 ± 0.2	$2.2^{+0.1}_{-0.2}$	$1.9^{+0.1}_{-0.2}$	$1.8^{+0.1}_{-0.2}$	2.2 ± 0.1	$1.8^{+0.2}_{-0.1}$	$1.7^{+0.2}_{-0.1}$
	i[a] (°)	⋯	68^{+1}_{-5}	⋯	⋯	67^{+4}_{-3}	⋯	⋯	67^{+2}_{-4}	⋯
	$R_{\rm in}$ (ISCO)	$1.01^{+0.06}_{-0.01}$	$1.06^{+0.09}_{-0.06}$	$1.07^{+0.03}_{-0.07}$	$1.01^{+0.14}_{-0.01}$	$1.05^{+0.11}_{-0.05}$	$1.11^{+0.04}_{-0.11}$	$1.02^{+0.06}_{-0.02}$	$1.09^{+0.06}_{-0.09}$	$1.03^{+0.08}_{-0.03}$
	$R_{\rm in}$ (R_g)	$6.06^{+0.36}_{-0.06}$	$6.36^{+0.54}_{-0.36}$	$6.42^{+0.18}_{-0.42}$	$6.06^{+0.84}_{-0.06}$	$6.30^{+0.66}_{-0.30}$	$6.66^{+0.24}_{-0.66}$	$6.12^{+0.36}_{-0.12}$	$6.54^{+0.36}_{-0.54}$	$6.18^{+0.48}_{-0.18}$
	kT_{bb} (keV)	$2.47^{+0.07}_{-0.04}$	$2.56^{+0.02}_{-0.03}$	$2.50^{+0.01}_{-0.05}$	$2.46^{+0.04}_{-0.08}$	$2.57^{+0.02}_{-0.03}$	$2.46^{+0.04}_{-0.01}$	$2.50^{+0.01}_{-0.11}$	$2.58^{+0.03}_{-0.04}$	$2.48^{+0.04}_{-0.02}$
	$\log(\xi)$	$1.51^{+0.07}_{-0.05}$	2.50 ± 0.03	$2.58^{+0.02}_{-0.05}$	$1.50^{+0.07}_{-0.05}$	$2.50^{+0.06}_{-0.05}$	$2.57^{+0.07}_{-0.03}$	$1.53^{+0.09}_{-0.07}$	$2.50^{+0.01}_{-0.06}$	2.57 ± 0.04
	$A_{\rm Fe}$[a]	⋯	$1.34^{+0.31}_{-0.01}$	⋯	⋯	1.4 ± 0.1	⋯	⋯	1.4 ± 0.1	⋯
	$\log(N)$[b] (cm^{-3})	$17.99^{+0.02}_{-0.18}$	$17.9^{+0.1}_{-0.2}$		$18.0^{+0.1}_{-0.2}$	$17.82^{+0.10}_{-0.08}$		$17.99^{+0.02}_{-0.13}$	$17.88^{+0.06}_{-0.24}$	
	$f_{\rm refl}$	$0.9^{+0.1}_{-0.2}$	$0.18^{+0.03}_{-0.01}$	0.13 ± 0.02	0.8 ± 0.1	$0.19^{+0.01}_{-0.02}$	0.13 ± 0.01	0.8 ± 0.1	$0.18^{+0.02}_{-0.03}$	$0.12^{+0.01}_{-0.02}$
	$\rm norm_{rel}$ (10^{-3})	$1.6^{+0.1}_{-0.2}$	3.2 ± 0.2	$3.7^{+0.2}_{-0.1}$	$1.72^{+0.03}_{-0.23}$	$3.1^{+0.2}_{-0.1}$	$3.87^{+0.04}_{-0.24}$	$1.6^{+0.1}_{-0.2}$	$3.2^{+0.2}_{-0.1}$	$3.8^{+0.1}_{-0.2}$
GAUSSIAN	E (keV)	⋯	...	⋯	...	$1.01^{+0.02}_{-0.04}$	1.03 ± 0.03	⋯	...	...
	σ (10^{-2} keV)	⋯	...	⋯	...	$8.5^{+0.8}_{-0.3}$	$8.1^{+1.3}_{-0.7}$	⋯	...	...
	$\rm norm_{gauss}$ (10^{-2})	....	⋯	...	⋯	$6.2^{+0.4}_{-0.8}$	$4.0^{+0.3}_{-0.5}$	⋯	...	...
	EW (eV)	⋯	...	⋯	...	17^{+1}_{-2}	15^{+1}_{-2}	⋯	...	...
MEKAL	kT (keV)	⋯	...	⋯	...	⋯	...	$1.54^{+0.19}_{-0.06}$	$1.37^{+0.11}_{-0.09}$	$1.36^{+0.13}_{-0.09}$
	$A_{\rm Fe}$[a]	⋯	...	⋯	...	⋯	...	⋯	$2.9^{+0.4}_{-0.3}$	⋯
	$\rm norm_{mekal}$ (10^{-2})	⋯	...	⋯	...	⋯	...	10^{+1}_{-2}	$11.0^{+0.8}_{-1.3}$	$9.1^{+1.3}_{-0.9}$
	$F_{\rm unabs,0.5-50\ keV}$	4.1 ± 0.6	2.5 ± 0.2	$2.1^{+0.2}_{-0.1}$	$4.0^{+0.2}_{-0.6}$	$2.5^{+0.3}_{-0.4}$	$2.1^{+0.2}_{-0.3}$	$4.1^{+0.6}_{-1.0}$	$2.5^{+0.3}_{-0.4}$	$2.0^{+0.4}_{-0.3}$
	χ^2 (dof)		1993.7 (1936)			1906.8 (1930)			1914.2 (1929)	

Notes. Errors are reported at the 90% confidence level. NICER is fit in the 0.5–10 keV energy band while NuSTAR is fit in the 3–30 keV band. A multiplicative constant is used on the NICER and FPMB data, while FPMA is fixed to unity. The outer disk radius is fixed at 1000 R_g and the dimensionless spin parameter is set to $a_* = 0$ (hence, 1 $R_{\rm ISCO} = 6\ R_g$). The density in the MEKAL model is fixed at 10^{15} cm^{-3}. The unabsorbed 0.5–50 keV flux, $F_{\rm unabs}$, 0.5–50 keV, is given in units of 10^{-8} erg s^{-1} cm^{-2}.

[a] Tied between all branches.

[b] Tied between HB and VX spectra.

Table 4
Reflection Modeling from Comptonization

Model	Parameter	RNS1			RNS2			RNS3		
		NB	VX	HB	NB	VX	HB	NB	VX	HB
CRABCOR	$C_{\rm FPMB}$	$1.022^{+0.002}_{-0.001}$	1.014 ± 0.002	$1.014^{+0.001}_{-0.002}$	1.022 ± 0.001	1.013 ± 0.002	$1.015^{+0.001}_{-0.003}$	$1.023^{+0.001}_{-0.002}$	$1.014^{+0.001}_{-0.002}$	1.014 ± 0.002
	$C_{\rm NICER}$	⋯	$0.964^{+0.013}_{-0.006}$	$0.991^{+0.014}_{-0.007}$	⋯	$0.969^{+0.009}_{-0.013}$	$0.998^{+0.007}_{-0.015}$	⋯	0.97 ± 0.01	1.00 ± 0.01
	$\Delta\Gamma_{\rm NICER}$ [b] (10^{-2})	⋯	$-6.1^{+0.9}_{-0.3}$		⋯	$-5.6^{+0.4}_{-0.9}$		⋯	$-5.6^{+0.5}_{-0.8}$	
TBFEO	$N_{\rm H}$ [a] (10^{21} cm^{-2})	⋯	$2.63^{+0.05}_{-0.13}$	⋯	⋯	2.59 ± 0.09	⋯	⋯	$2.51^{+0.13}_{-0.02}$	⋯
	$A_{\rm O}$ [a]	⋯	$1.46^{+0.09}_{-0.06}$	⋯	⋯	$1.46^{+0.07}_{-0.10}$	⋯	⋯	$1.49^{+0.05}_{-0.09}$	⋯
DISKBB	$kT_{\rm in}$ (keV)	1.78 ± 0.01	$1.718^{+0.03}_{-0.01}$	$1.69^{+0.03}_{-0.01}$	$1.76^{+0.05}_{-0.03}$	$1.74^{+0.02}_{-0.01}$	$1.71^{+0.01}_{-0.04}$	$1.78^{+0.01}_{-0.04}$	$1.74^{+0.01}_{-0.03}$	1.70 ± 0.03
	$\rm norm_{disk}$	85 ± 3	78^{+1}_{-5}	51^{+2}_{-3}	86^{+5}_{-7}	76^{+3}_{-4}	49^{+5}_{-1}	83^{+6}_{-4}	77^{+5}_{-2}	51 ± 3
NTHCOMP	Γ	2.02 ± 0.03	$1.66^{+0.05}_{-0.02}$	$1.73^{+0.02}_{-0.01}$	$2.00^{+0.09}_{-0.05}$	$1.67^{+0.04}_{-0.02}$	$1.74^{+0.01}_{-0.03}$	$2.04^{+0.02}_{-0.08}$	1.65 ± 0.03	$1.72^{+0.03}_{-0.02}$
	kT_e (keV)	$2.85^{+0.07}_{-0.03}$	$2.80^{+0.08}_{-0.01}$	$2.88^{+0.05}_{-0.02}$	$2.75^{+0.24}_{-0.05}$	2.87 ± 0.04	$2.93^{+0.04}_{-0.05}$	$2.83^{+0.12}_{-0.09}$	$2.83^{+0.05}_{-0.08}$	$2.90^{+0.05}_{-0.03}$
	kT_{bb} (10^{-1} keV)	1.0 ± 0.2	$0.8^{+0.2}_{-0.1}$	$0.95^{+0.22}_{-0.03}$	$1.1^{+0.2}_{-0.3}$	$0.85^{\dagger}$	1.0 ± 0.2	$1.39^{+0.58}_{-0.03}$	$0.85^{\dagger}$	$1.11^{+0.07}_{-0.22}$
	$\rm norm_{nth}$	2.8 ± 0.2	1.0 ± 0.1	$1.30^{+0.06}_{-0.08}$	2.9 ± 0.3	$0.96^{+0.13}_{-0.06}$	$1.29^{+0.05}_{-0.11}$	$2.85^{+0.09}_{-0.47}$	$0.91^{+0.10}_{-0.08}$	$1.21^{+0.10}_{-0.04}$
RDBLUR	$\lvert -$ Betor10$\rvert$	$1.5^{+0.1}_{-0.5}$	$1.5^{+0.1}_{-0.5}$	$1.6^{+0.1}_{-0.3}$	$2.3^{+0.2}_{-0.8}$	$1.3^{+0.1}_{-0.3}$	$1.2^{+0.3}_{-0.2}$	$1.9^{+0.2}_{-0.6}$	$1.4^{+0.4}_{-0.2}$	$1.4^{+0.3}_{-0.2}$
	$R_{\rm in}$ (R_g)	6.7 ± 0.7	$6.4^{+0.6}_{-0.4}$	$6.3^{+1.3}_{-0.3}$	$6.6^{+1.3}_{-0.6}$	$6.6^{+0.8}_{-0.6}$	$6.5^{+0.7}_{-0.5}$	$6.3^{+1.1}_{-0.3}$	$6.3^{+1.1}_{-0.3}$	$7.0^{+1.5}_{-1.0}$
	i [a] (°)	⋯	63^{+4}_{-3}	⋯	⋯	61^{+2}_{-11}	⋯	⋯	64^{+6}_{-7}	⋯
RFXCONV	$rel_{\rm refl}$	$1.0^{+0.1}_{-0.2}$	0.27 ± 0.05	$0.14^{+0.04}_{-0.02}$	$1.1^{+0.1}_{-0.3}$	$0.25^{+0.02}_{-0.05}$	$0.12^{+0.04}_{-0.02}$	$1.2^{+0.1}_{-0.3}$	$0.26^{+0.07}_{-0.06}$	$0.14^{+0.01}_{-0.03}$
	$A_{\rm Fe}$ [a]	—	$2.0^{+0.2}_{-0.4}$	⋯	⋯	$1.8^{+0.2}_{-0.5}$	⋯	⋯	$1.7^{+0.5}_{-0.2}$	⋯
	$\log(\xi)$	$2.15^{+0.17}_{-0.05}$	$2.67^{+0.04}_{-0.17}$	$2.83^{+0.07}_{-0.12}$	$1.8^{+0.5}_{-0.1}$	2.6 ± 0.1	2.9 ± 0.1	$2.11^{+0.15}_{-0.07}$	$2.60^{+0.13}_{-0.08}$	$2.81^{+0.11}_{-0.05}$
GAUSSIAN	E (keV)	⋯	...	⋯	...	$1.02^{+0.08}_{-0.05}$	$1.03^{+0.03}_{-0.06}$	⋯	...	...
	σ (10^{-2} keV)	⋯	...	⋯	...	6 ± 2	5 ± 1	⋯	...	...
	$\rm norm_{gauss}$ (10^{-2})	⋯	...	⋯	...	$1.8^{+0.3}_{-0.4}$	$1.3^{+0.3}_{-0.2}$	⋯	...	...
	EW (eV)	⋯	...	⋯	...	7^{+2}_{-1}	6 ± 1	⋯	...	...
MEKAL	kT (keV)	⋯	...	⋯	...	⋯	...	$1.9^{+0.2}_{-0.6}$	1.1 ± 0.3	$1.5^{+0.3}_{-0.4}$
	$A_{\rm Fe}$	⋯	...	⋯	...	⋯	...	⋯	$1.9^{+0.6}_{-0.5}$	⋯
	$\rm norm_{mekal}$ (10^{-2})	⋯	...	⋯	...	⋯	...	$0.9^{+0.6}_{-0.3}$	$4.3^{+0.9}_{-1.2}$	$4.1^{+1.0}_{-1.2}$
	$F_{\rm unabs,0.5-50\ keV}$	3.4 ± 0.3	$2.3^{+0.2}_{-0.3}$	$1.9^{+0.1}_{-0.2}$	3.4 ± 0.4	2.3 ± 0.5	$1.9^{+0.5}_{-0.3}$	$3.3^{+2.2}_{-1.2}$	$2.3^{+0.6}_{-0.7}$	$1.9^{+0.5}_{-0.6}$
	χ^2 (dof)		2024.9 (1938)			2009.7 (1933)			2006.4 (1932)	

Notes. Errors are reported at the 90% confidence level. NICER is fit in the 0.5–10 keV energy band, while NuSTAR is fit in the 3–30 keV band. A multiplicative constant is used on the NICER and FPMB data, while FPMA is fixed to unity. The outer disk radius is fixed at 1000 R_g and the dimensionless spin parameter is set to $a_* = 0$ (hence, 1 $R_{\rm ISCO} = 6\ R_g = 12.4$ km). The density in the MEKAL model is fixed at 10^{15} cm^{-3}. The unabsorbed 0.5–50 keV flux, $F_{\rm unabs}$, 0.5–50 keV, is given in units of 10^{-8} erg s^{-1} cm^{-2}. The inclination parameter is tied between the RDBLUR and RFXCONV convolutions.

[a] Tied between all branches.

[b] Tied between HB and VX spectra; † = fixed.

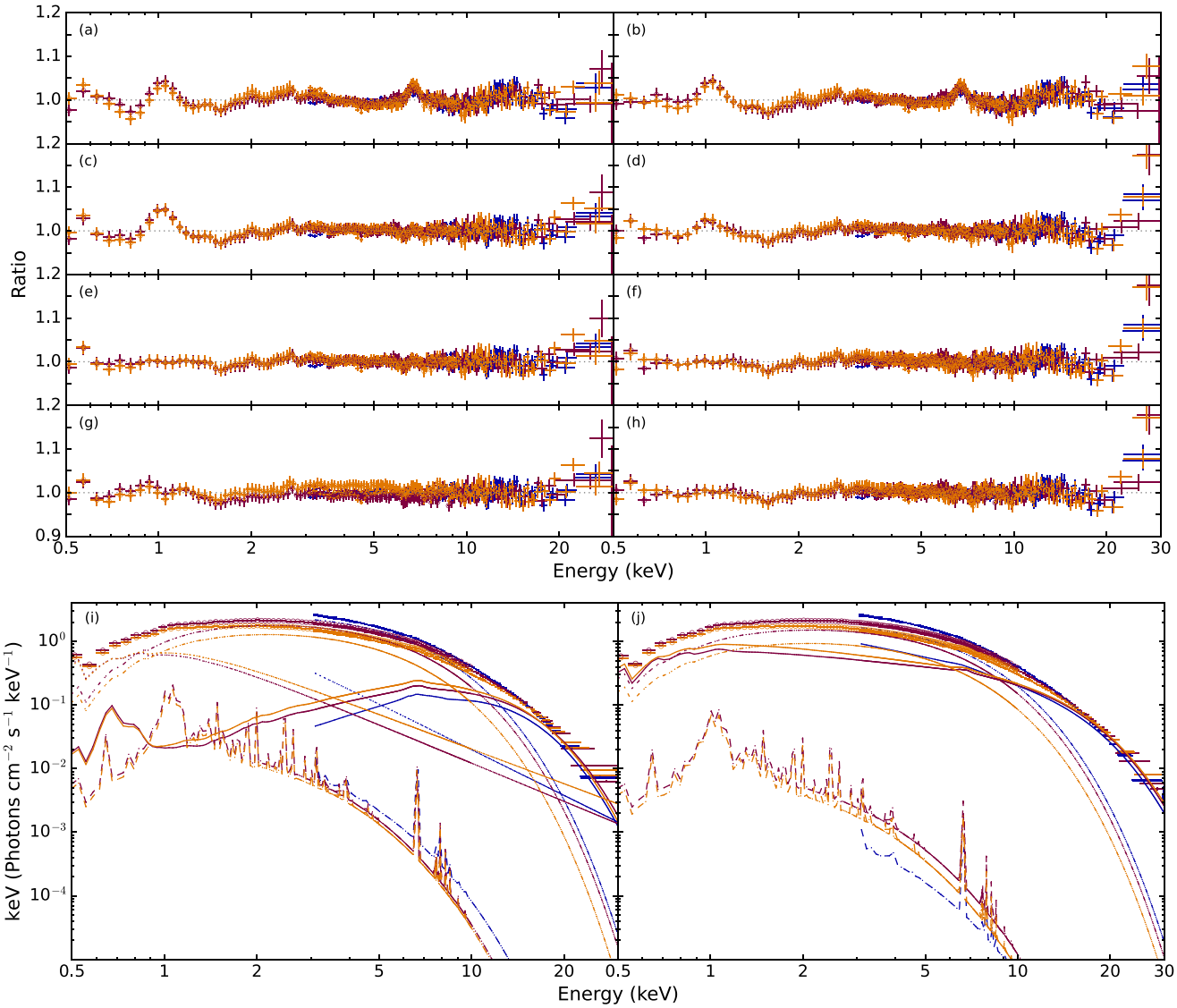

Figure 3. The ratios of the data to the models reported in Tables 2–4, where the panels correspond to (a) C1; (b) C2; (c) RNS1; (d) RFX1; (e) RNS2; (f) RFX2; (g) RNS3; and (h) RFX3. Blue indicates the NB from Obs1, maroon is the VX from Obs2, and orange is the HB from Obs3. Data were rebinned for plotting purposes. Panels (i) and (j) show the unfolded spectra and model components for RNS3 and RFX3, respectively. The dotted–dashed line is the disk component, the dotted line is the power-law component, the dashed line is the collisional plasma, and the solid line indicates the reflection model with the corresponding illuminating component included.

abundance ($A_{\rm Fe}$), the inclination angle ($\cos(i)$), redshift (z), and an ionization parameter ($\log(\xi)$). The parameters of the relativistic blurring kernal RDBLUR are the emissivity index (Betor10: $R^{\rm Betor10}$), the inner disk radius in R_g, the outer disk radius, and inclination (i). The outer disk radius is fixed at 1000 R_g, to be consistent with RELXILLNS, and the inclination parameters are tied between RDBLUR and RFXCONV for consistency. We report the parameter values for this fit in Table 4 under "RFX1."

The 1 keV feature is still present in the spectrum regardless of the reflection model utilized (see panels (c) and (d) of Figure 3). We proceed to model the 1 keV feature in the NICER data with a Gaussian emission line (GAUSS) to determine the line centroid energy and equivalent width. These fits are reported as "RNS2" and "RFX2" in Tables 3 and 4, while the ratios of the overall models to the data are shown in Figure 3(e) and (f), respectively. The addition of the Gaussian line improves the fit by 8.2σ when using RELXILLNS, but provides a marginal 2.5σ improvement from RFX1 to RFX2. We note that the seed photon temperature of the Comptonization model tends to an unphysically low value ($kT_{bb} \leqslant 8$ eV) in the VX branch with the addition of the Gaussian line, therefore we fix this parameter to the median value from RFX1. This was not an issue in the HB due to the NICER spectrum containing 4.8×10^6 more counts than in the VX. All of the parameter values are consistent within the 90% confidence level when kT_{bb} is left free or fixed, hence this parameter does not have a notable impact on the results. Although the feature is present regardless of continuum and reflection modeling, the inferred equivalent width is smaller in RFX2, which may be due to the low-energy turnover in the Comptonization model. Additionally, the strength of the emission line does appear to change with flux as reported by Vrtilek et al. (1986). Indeed, the energy of this line is too low to

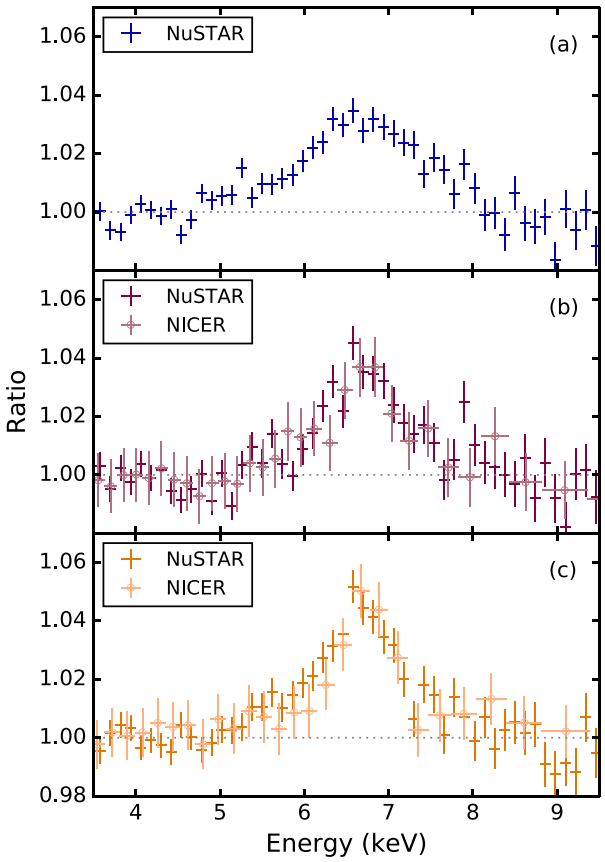

Figure 4. The ratios of the data in the Fe K band to the continuum model C1 for (a) NB, (b) VX, and (c) HB. Only one NuSTAR FPM is shown for clarity. Data were rebinned for plotting purposes.

originate from the relativistic reflection component like the Fe L emission in Serpens X-1 (Ludlam et al. 2018). It could be a blend of Fe, Ni, and O transition lines, which originate from collisionally ionized material far from the inner region of the accretion disk as proposed by Vrtilek et al. (1986).

We proceed to replace the Gaussian emission line component for a collisionally ionized plasma model MEKAL (Mewe et al. 1985, 1986; Liedahl et al. 1995) to determine how this interpretation impacts the inferred inner disk radius. The density of the material is fixed at 10^{15} cm^{-3} (Schulz et al. 2009) and the abundance of the plasma is tied between the spectra. The temperature and normalization are free to vary. This fit is referred to as "RNS3" and "RFX3" in Tables 3 and 4. Again, the seed photon temperature of the Comptonization component tended to an unphysical value of $kT_{bb} \leqslant 3$ eV in the RFX3 VX branch and was fixed at the median value from RFX1. However, the results with this parameter fixed agree within the 90% confidence level when kT_{bb} was free to vary. The ratios of the models to the data are shown in Figure 3(g) and (h), respectively. The addition of a MEKAL component represents 7.6σ and 2.7σ improvements in comparison to RNS1 and RFX1, respectively. Figure 3(i) and (j) show the unfolded spectra with the model components for RNS3 and RFX3, respectively. The MEKAL model predicts a narrow emission line in the Fe K band as well, but this is orders of magnitude below the broadened emission line from reflection. The normalization of the MEKAL component for the NB in RFX3 is lower in comparison to the VX and HB, but this could be due to the lack of NICER data to anchor the component through modeling of the 1 keV feature. The exact nature of the 1 keV component is beyond the scope of this paper, but regardless of how the feature is modeled the inner disk radius still remains close to the NS.

4. Discussion

We present an analysis of the reflection spectrum in Cyg X-2 using three NuSTAR and two simultaneous NICER observations. The source traced out the flaring to the horizontal branch within these observations. The data were divided into the respective branches and spectra with $\geqslant 10^6$ cumulative counts were modeled according to different continuum conventions. This resulted in spectra of the source in the NB from the first NuSTAR observation, the VX between the NB and HB during the second NuSTAR observation, and the HB in the third NuSTAR observation. Simultaneous NICER spectra were extracted for the VX and HB allowing for spectral modeling from 0.5–30 keV. The reflection spectrum was modeled with RELXILLNS and RFXCONV depending on the illuminating continuum component. Regardless of which reflection model was utilized, the inner disk radius remained close to $R_{\rm ISCO}$ ($1\,R_{\rm ISCO} = 6\,R_g$ for $a = 0$).

The inferred inclination from reflection modeling (RELXILLNS: $i = 67° \pm 4°$; RDBLUR*RFXCONV: $i = 60° \pm 10°$) is consistent with the optical results ($i = 62.°5 \pm 4°$: Orosz & Kuulkers 1999), but conflicts with the previously reported low inclinations from reflection modeling in Cackett et al. (2010) and Mondal et al. (2018). Again, one possible explanation could be the material farther out partially obscuring the blue-wing emission of the Fe K line (Taylor & Reynolds 2018) at the time of the Suzaku observation reported in Cackett et al. (2010). This effect has been invoked to explain conflicting inclination measurements between reflection modeling and dynamical estimates in the black hole X-ray binary XTE J1550-564 (Connors et al. 2019). In the case of the Mondal et al. (2018) study that utilized the same NuSTAR observation from 2015, the differences between the results reported therein and here could be due to differences in how the data were reduced (e.g., the bright source flag expression in "nupipeline") and handled (e.g., our self-consistent reflection modeling and choice to tie various parameters across observations). The inclination varies more when using RFXCONV than RELXILLNS, but this is likely due to the differences in the relativistic convolution routines within each model, as discussed in Ludlam et al. (2020). Further differences between the models may be due to the hard-coded disk density in RFXCONV of 10^{15} cm^{-3}, while the RELXILLNS model has a variable disk density component that allows for conditions closer to the physical density expected in accretion disks of LMXBs. The hard-coded lower disk density in RFXCONV is likely responsible for the higher inferred iron abundance, $A_{\rm Fe}$, in comparison to the results from RELXILLNS, which are closer to solar abundances.

The emissivity indices are lower than the $q = 3$ profile for Euclidean geometry, but are close to the expected shallower illumination profile from an extended disk corona around a slowly spinning compact object (Kinch et al. 2016, 2019). The ionization parameter is consistent with the value reported in Cackett et al. (2010), but higher than those found in Mondal et al. (2018). The Mondal et al. (2018) study also found subsolar Fe abundances, which may explain the lower inferred ionization since positive correlations between $\log(\xi)$ and $A_{\rm Fe}$ have been observed previously when modeling reflection in

Table 5
Radial Estimates from Spectral Modeling

Model	Branch	$R_{\rm in,diskbb}$	$R_{\rm bbody,spherical}$	$R_{\rm bbody,banded}$	$R_{\rm in,reflection}$	$R_{\rm BL,max}$
C1	NB	46 ± 16	6 ± 2	19 ± 6	⋯	68 ± 23
	VX	39 ± 13	6 ± 2	19 ± 3	⋯	26 ± 9
	HB	33 ± 11	6 ± 2	20 ± 7	⋯	19 ± 7
C2	NB	39 ± 15	⋯	...	⋯	42 ± 14
	VX	31 ± 12	...	⋯	...	32 ± 11
	HB	24 ± 9	...	⋯	...	27 ± 11
RNS1	NB	45 ± 15	⋯	...	15.6 ± 2.0	50 ± 18
	VX	41 ± 14	⋯	...	16.3 ± 2.2	25 ± 12
	HB	37 ± 13	...	...	15.9 ± 2.1	19 ± 7
RNS2	NB	46 ± 15	⋯	...	16.3 ± 2.2	48 ± 18
	VX	41 ± 14	⋯	...	16.3 ± 2.3	25 ± 9
	HB	39^{+13}_{-14}	...	⋯	16.3 ± 2.2	19 ± 7
RNS3	NB	45 ± 15	⋯	...	15.7 ± 2.0	50 ± 21
	VX	40 ± 14	...	⋯	16.3 ± 2.2	25 ± 9
	HB	38 ± 13	⋯	...	16.0 ± 2.1	18 ± 7
RFX1	NB	34 ± 13	⋯	...	16.9 ± 2.7	48 ± 16
	VX	33 ± 12	⋯	...	$16.1^{+2.5}_{-2.2}$	32 ± 11
	HB	27 ± 10	⋯	...	$15.9^{+3.8}_{-2.1}$	27 ± 9
RFX2	NB	35 ± 13	⋯	...	$16.6^{+3.9}_{-2.5}$	48 ± 17
	VX	33 ± 12	⋯	...	$16.6^{+2.9}_{-2.5}$	32 ± 13
	HB	26 ± 10	⋯	...	$16.4^{+2.7}_{-2.4}$	27 ± 11
RFX3	NB	34 ± 13	⋯	...	$15.9^{+3.4}_{-2.1}$	46^{+34}_{-23}
	VX	33 ± 12	⋯	...	$15.9^{+3.4}_{-2.1}$	32 ± 14
	HB	27 ± 10	⋯	...	$17.6^{+4.4}_{-3.3}$	27 ± 12

Note. All values are given in units of km. The inner disk radius from reflection modeling was converted into km assuming an NS mass of $M_{\rm NS} = 1.71 \pm 0.21\ M_\odot$ (and $a_* = 0$ in the case of the values taken from Table 3). The estimates encompass the entire reported distance range to the source (9.15 ± 3.05 kpc). A color correction factor of $f_{\rm cor} = 1.7$ (Shimura & Takahara 1995) was used when converting the normalization of the DISKBB and BBODY components into their emitting radius. $R_{\rm BL,max}$ is the radial extent of the boundary layer from the surface of the NS using equation (25) from Popham & Sunyaev (2001). For C1 and the fits labeled RNS, the inclination range from fitting RELXILLNS was used ($i = 67° \pm 4°$). For C2 and the fits labeled RFX, the inclination range from fitting RDBLUR*RFXCONV was used ($i = 60° \pm 10°$).

X-ray binaries (e.g., Connors et al. 2019). Our choice to tie the $A_{\rm Fe}$ between observations reduces the degeneracy while allowing the $\log(\xi)$ to be a free parameter.

4.1. Radius Constraints

Apart from the inner disk radius returned by the reflection model components, we can calculate the inferred emission radius from the normalizations of the thermal disk component (DISKBB) and single-temperature blackbody (BBODY). The emitting blackbody radius is given assuming both a spherical and a narrowband emission region on the surface of the NS with a vertical height that is 10% of the radial extent (Popham & Sunyaev 2001; Ludlam et al. 2021). Additionally, we can calculate the maximum radial extent of a boundary layer extending from the surface of the NS based on the mass accretion rate from Equation (25) in Popham & Sunyaev (2001) for comparison. It is important to note that the maximum radial extent using this equation does not account for the spreading of the boundary layer in the vertical direction or effects from the rotation of the NS. We report these values in Table 5 in units of km for each spectral model reported in Tables 2–4 and branch. The implausibly small inferred emitting radius of the blackbody component when assuming spherical emission supports the presence of a narrowband emission region (Inogamov & Sunyaev 1999). The inner disk radius inferred from the disk component is larger than that inferred from the reflection modeling. The choice of spectral hardening factor does impact the inferred radius (e.g., Kubota et al. 2001). However, the inferred DISKBB radius is also known to be up to a factor of ∼2.2 smaller when accounting for the zero-torque inner boundary condition expected for thin disk accretion (Zimmerman et al. 2005). This brings the inner disk radius values from the DISKBB component within the uncertainty of the reflection model. The relative agreement between the inferred radius measurements of each of these components is an encouraging cross-check on the validity of the overall spectral modeling results.

4.2. M–R Plane

Given that the inner accretion disk is close to the $R_{\rm ISCO}$ in all cases, we explore the constraints that this translates to on the M–R plane for NSs, and hence the EoS of ultradense, cold matter. The radius of the ISCO around a compact object in units of gravitational radii is dependent upon the dimensionless spin parameter, $a = cJ/GM^2$, of the compact object (Bardeen et al. 1972). The spin therefore enables a translation from ISCO to gravitational radii. This can then be converted into kilometers given the NS mass estimate of $1.71 \pm 0.21\ M_\odot$ for Cyg X-2 (Casares et al. 2010). Figure 5 plots the range that the more conservative constraints from RELXILLNS of $R_{\rm in} \leqslant 1.15\ R_{\rm ISCO}$ for $a = 0$ correspond to on the M–R plane used to characterize the EoS. Note that a higher spin value corresponds to a smaller gravitational radius for $R_{\rm ISCO}$, therefore we are presenting the most conservative upper limit when using $a = 0$. This is then compared to the M–R estimates from gravitational wave signatures of binary NS and pulsar lightcurve modeling.

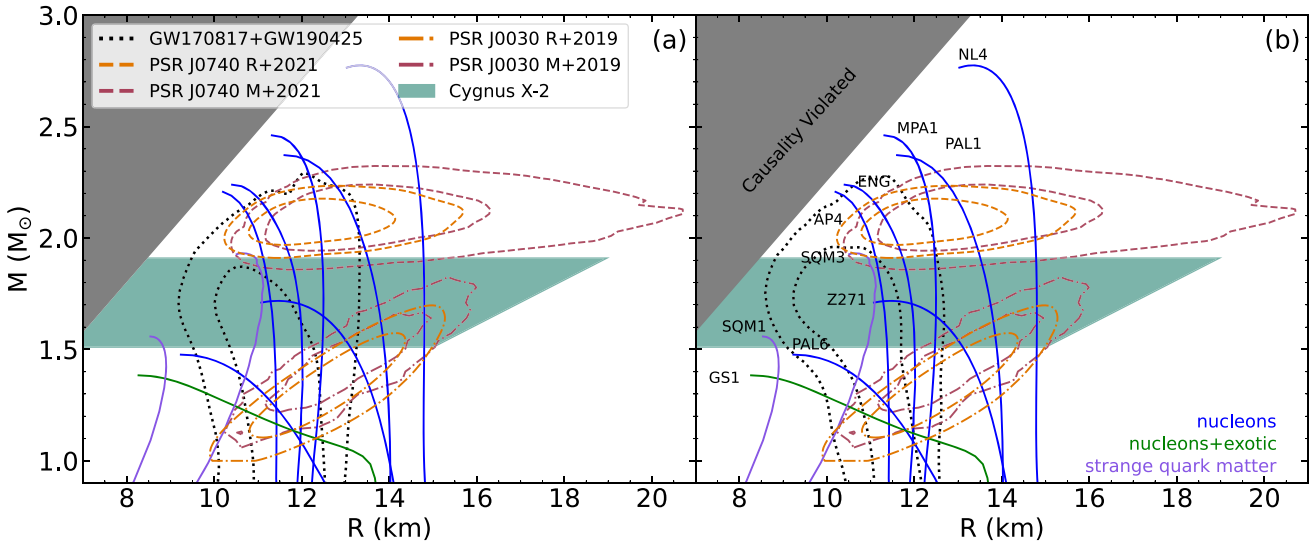

Figure 5. Mass and radius constraints from NS gravitational wave events and NICER pulsar lightcurve modeling in comparison to reflection modeling of Cyg X-2. The panels differ by the *M*–*R* constraints from the combined GW170817 (Abbott et al. 2019) and GW190425 (The LIGO Scientific Collaboration et al. 2020) signatures using (a) a piecewise polytropic model and (b) a speed-of-sound model through a Bayesian framework as reported in Raaijmakers et al. (2021). These are denoted by the black dotted line. The solid cyan region indicates the conservative radius constraints for Cyg X-2, based on the reflection modeling reported in Table 3. The solid gray region indicates where causality is violated (i.e., the sound speed within the NS exceeds the speed of light). Select EoSs from Lattimer & Prakash (2001) are shown to demonstrate the behavior on the *M*–*R* plane for a given internal composition. Pulsar lightcurve modeling of NICER data for PSR J0740+6620 is indicated by dashed lines from Riley et al. (2021) (R+2021: orange) and Miller et al. (2021) (M+2021: maroon). The dotted–dashed lines indicate the results for lightcurve modeling of PSR J0030+0452 reported in Riley et al. (2019; R+2019: orange) and Miller et al. (2019; M+2019: maroon). Confidence contours correspond to the 68% and 95% credible regions.

The combined gravitational wave constraints from the double NS mergers GW170817 (Abbott et al. 2019) and GW190425 (The LIGO Scientific Collaboration et al. 2020) are determined through a Bayesian framework as reported in Raaijmakers et al. (2021) for both a piecewise polytropic model (Figure 5(a)) and a speed-of-sound model (Figure 5(b)). Additionally, the NICER pulsar lightcurve modeling results for PSR J0030 +0425 (Riley et al. 2019; Miller et al. 2019) and PSR J0740 +6620 (Riley et al. 2021; Miller et al. 2021) are shown. The allowed region on the *M*–*R* plane for Cyg X-2 could be further narrowed down in the future by obtaining improved mass constraints with better optical lightcurve data and ellipsoidal modeling. Disk reflection is able to provide an upper limit on the NS radii but it is not able to rule out plausible EoSs on its own. Each of these methods have their own systematic uncertainties (see the discussions in Ludlam et al. 2017; Riley et al. 2019; Miller et al. 2019; Raaijmakers et al. 2021, and references therein), but they can provide independent checks of constraints from the others on the *M*–*R* plane.

5. Conclusion

We perform a spectral analysis of NuSTAR and NICER observations of Cygnus X-2 while the source was in the normal branch, the vertex, and the horizontal branch in order to constrain the inner disk radius via reflection modeling. A broad Fe line component was detected in all states, as well as a 1 keV emission line where NICER data was available. The reflection spectrum was modeled in two different ways assuming (1) an illuminating blackbody component, and (2) a Comptonization thermal component. The low-energy emission line was not able to be modeled by the reflection component, suggesting that it originated farther out in the accretion disk. Regardless of the reflection model utilized, or how the 1 keV feature was accounted for, the inner disk radius remained close to the NS. We utilized these measurements to place an upper limit on the radius of the NS. When taken in comparison to state-of-the-art methods, disk reflection can provide an independent check of constraints on the *M*–*R* plane.

Support for this work was provided by NASA through the NASA Hubble Fellowship grant #HST-HF2-51440.001 awarded by the Space Telescope Science Institute, which is operated by the Association of Universities for Research in Astronomy, Incorporated, under NASA contract NAS5-26555. This research has made use of the NuSTAR Data Analysis Software (NuSTARDAS) jointly developed by the ASI Science Data Center (ASDC, Italy) and the California Institute of Technology (Caltech, USA).

J.A.G. acknowledges support from NASA grant 80NSSC20K0540 and from the Alexander von Humboldt Foundation. S.G. acknowledges the support of the Centre National d'Etudes Spatiales (CNES).

ORCID iDs

R. M. Ludlam https://orcid.org/0000-0002-8961-939X
E. M. Cackett https://orcid.org/0000-0002-8294-9281
J. A. García https://orcid.org/0000-0003-3828-2448
A. L. Stevens https://orcid.org/0000-0002-5041-3079
A. C. Fabian https://orcid.org/0000-0002-9378-4072
J. Homan https://orcid.org/0000-0001-8371-2713
M. Ng https://orcid.org/0000-0002-0940-6563
S. Guillot https://orcid.org/0000-0002-6449-106X
D. Chakrabarty https://orcid.org/0000-0001-8804-8946

References

Abbott, B. P., Abbott, R., Abbott, T. D., et al. 2019, PhRvX, 9, 011001
Bałucińska-Church, M., Gibiec, A., Jackson, N. K., & Church, M. J. 2010, A&A, 512, A9

Bałucińska-Church, M., Schulz, N. S., Wilms, J., et al. 2011, A&A, 530, A102
Bardeen, J. M., Press, W. H., & Teukolsky, S. A. 1972, ApJ, 178, 347
Byram, E. T., Chubb, T. A., & Friedman, H. 1966, AJ, 71, 379
Cackett, E. M., Miller, J. M., Ballantyne, D. R., et al. 2010, ApJ, 720, 205
Cackett, E. M., Miller, J. M., Bhattacharyya, S., et al. 2008, ApJ, 674, 415
Casares, J., Charles, P., & Kuulkers, E. 1998, ApJL, 493, L39
Casares, J., González Hernández, J. I., Israelian, G., & Rebolo, R. 2010, MNRAS, 401, 2517
Chiappetti, L., Treves, A., Branduardi-Raymont, G., et al. 1990, ApJ, 361, 596
Connors, R. M. T., García, J. A., Steiner, J. F., et al. 2019, ApJ, 882, 179
Cowley, A. P., Crampton, D., & Hutchings, J. B. 1979, ApJ, 231, 539
Di Salvo, T., Farinelli, R., Burderi, L., et al. 2002, A&A, 386, 535
Ding, H., Deller, A. T., & Miller-Jones, J. C. A. 2021, PASA, 38, e048
Done, C., & Gierlínski, M. 2006, MNRAS, 367, 659
Fabian, A. C., Iwasawa, K., Reynolds, C. S., & Young, A. J. 2000, PASP, 112, 1145
Fabian, A. C., Rees, M. J., Stella, L., & White, N. E. 1989, MNRAS, 238, 729
Farinelli, R., Paizis, A., Landi, R., & Titarchuk, L. 2009, A&A, 498, 509
Fridriksson, J. K., Homan, J., & Remillard, R. A. 2015, ApJ, 809, 52
Galloway, D. K., Muno, M. P., Hartman, J. M., Psaltis, D., & Chakrabarty, D. 2008, ApJS, 179, 360
García, J., Dauser, T., Lohfink, A., et al. 2014, ApJ, 782, 76
García, J. A., Dauser, T., Ludlam, R., et al. 2022, ApJ, 926, 13
Hasinger, G., & van der Klis, M. 1989, A&A, 225, 79
HI4PI Collaboration, Ben Bekhti, N., Flöer, L., et al. 2016, A&A, 594, A116
Inogamov, N. A., & Sunyaev, R. A. 1999, AstL, 25, 269
Kahn, S. M., & Grindlay, J. E. 1984, ApJ, 281, 826
Kinch, B. S., Schnittman, J. D., Kallman, T. R., & Krolik, J. H. 2016, ApJ, 826, 52
Kinch, B. S., Schnittman, J. D., Kallman, T. R., & Krolik, J. H. 2019, ApJ, 873, 71
Kubota, A., Makishima, K., & Ebisawa, K. 2001, ApJL, 560, L147
Kuulkers, E., Parmar, A. N., Owens, A., Oosterbroek, T., & Lammers, U. 1997, A&A, 323, L29
Kuulkers, E., van der Klis, M., & Vaughan, B. A. 1996, A&A, 311, 197
Lattimer, J. M., & Prakash, M. 2001, ApJ, 550, 426
Liedahl, D. A., Osterheld, A. L., & Goldstein, W. H. 1995, ApJ, 438, 115
Lin, D., Remillard, R. A., & Homan, J. 2007, ApJ, 667, 1073
Ludlam, R. M., Cackett, E. M., García, J. A., et al. 2020, ApJ, 895, 45
Ludlam, R. M., Jaodand, A. D., García, J. A., et al. 2021, ApJ, 911, 123
Ludlam, R. M., Miller, J. M., Arzoumanian, Z., et al. 2018, ApJL, 858, L5
Ludlam, R. M., Miller, J. M., Bachetti, M., et al. 2017, ApJ, 836, 140
Magdziarz, P., & Zdziarski, A. 1995, MNRAS, 273, 837
Mewe, R., Gronenschild, E. H. B. M., & van den Oord, G. H. J. 1985, A&AS, 62, 197
Mewe, R., Lemen, J. R., & van den Oord, G. H. J. 1986, A&AS, 65, 511
Miller, J. M., Maitra, D., Cackett, E. M., Bhattacharyya, S., & Strohmayer, T. E. 2011, ApJL, 731, L7
Miller, M. C., Lamb, F. K., Dittmann, A. J., et al. 2019, ApJL, 887, L24
Miller, M. C., Lamb, F. K., Dittmann, A. J., et al. 2021, ApJL, 918, L28
Mitsuda, K., Inoue, H., Koyama, K., et al. 1984, PASJ, 36, 741
Mondal, A. S., Dewangan, G. C., Pahari, M., & Raychaudhuri, B. 2018, MNRAS, 474, 2064
Orosz, J. A., & Kuulkers, E. 1999, MNRAS, 305, 1320
Özel, F., & Freire, P. 2016, ARA&A, 54, 401
Popham, R., & Sunyaev, R. 2001, ApJ, 547, 355
Psaradaki, I., Costantini, E., Mehdipour, M., et al. 2020, A&A, 642, 208
Raaijmakers, G., Greif, S. K., Hebeler, K., et al. 2021, ApJL, 918, L29
Remillard, R. A., Loewenstein, M., Steiner, J. F., et al. 2022, AJ, 163, 130
Riley, T. E., Watts, A. L., Bogdanov, S., et al. 2019, ApJL, 887, L21
Riley, T. E., Watts, A. L., Ray, P. S., et al. 2021, ApJL, 918, L27
Ross, R. R., & Fabian, A. C. 2005, MNRAS, 358, 211
Schulz, N. S., Huenemoerder, D. P., Ji, L., et al. 2009, ApJL, 692, L80
Shaposhnikov, N., Titarchuk, L., & Laurent, P. 2009, ApJ, 699, 1223
Shimura, T., & Takahara, R. 1995, ApJ, 445, 780
Smale, A. P. 1998, ApJL, 498, L141
Smale, A. P., Done, C., Mushotzky, R. F., et al. 1993, ApJ, 410, 796
Steiner, J. F., McClintock, J. E., Remillard, R. A., et al. 2010, ApJL, 718, L117
Taylor, C., & Reynolds, C. S. 2018, ApJ, 855, 120
The LIGO Scientific Collaborationthe Virgo Collaboration, Abbott, B. P., et al. 2020, ApJL, 892, L3
Verner, D. A., Ferland, G. J., Korista, K. T., & Yakovlev, D. G. 1996, ApJ, 465, 487
Vrtilek, S. D., Kahn, S. M., Grindlay, J. E., Helfand, D. J., & Seward, F. D. 1988, ApJ, 329, 276
Vrtilek, S. D., Swank, J. H., Kelley, R. L., & Kahn, S. M. 1986, ApJ, 307, 69
Wijnands, R., & van der Klis, M. 2001, MNRAS, 321, 537
Wijnands, R., van der Klis, M., Kuulkers, E., Asai, K., & Hasinger, G. 1997, A&A, 323, 399
Wilms, J., Allen, A., & McCray, R. 2000, ApJ, 542, 914
Zdziarski, A. A., Johnson, W. N., & Magdziarz, P. 1996, MNRAS, 283, 193
Zimmerman, E. R., Narayan, R., McClintock, J. E., & Miller, J. M. 2005, ApJ, 618, 832
Zycki, P. T., Done, C., & Smith, D. A. 1999, MNRAS, 309, 561